Photoacoustic imaging of fluorophores using pump-probe excitation

Julia Märk,[1,*] Franz-Josef Schmitt,[2] Christoph Theiss,[1] Hakan Dortay,[1] Thomas Friedrich,[2] and Jan Laufer[1,3]

[1]*Institut für Optik und Atomare Physik, Technische Universität Berlin, Strasse des 17. Juni 135, 10623 Berlin, Germany*
[2]*Institut für Chemie, Technische Universität Berlin, Strasse des 17. Juni 135, 10623 Berlin, Germany*
[3]*Institut für Radiologie, Charité – Universitätsmedizin Berlin, Charitéplatz 1, 10117 Berlin, Germany*
[*]*julia.maerk@tu-berlin.com*

Abstract: A pump-probe technique for the detection of fluorophores in tomographic PA images is introduced. It is based on inducing stimulated emission in fluorescent molecules, which in turn modulates the amount of thermalized energy, and hence the PA signal amplitude. A theoretical model of the PA signal generation in fluorophores is presented and experimentally validated on cuvette measurements made in solutions of Rhodamine 6G, a fluorophore of known optical and molecular properties. The application of this technique to deep tissue tomographic PA imaging is demonstrated by determining the spatial distribution of a near-infrared fluorophore in a tissue phantom.

References and links

1. P. Beard, "Biomedical photoacoustic imaging," Interface Focus **1**(4), 602–631 (2011).
2. L. V. Wang and S. Hu, "Photoacoustic tomography: in vivo imaging from organelles to organs," Science **335**(6075), 1458–1462 (2012).
3. N. C. Deliolanis, A. Ale, S. Morscher, N. C. Burton, K. Schaefer, K. Radrich, D. Razansky, and V. Ntziachristos, "Deep-tissue reporter-gene imaging with fluorescence and optoacoustic tomography: a performance overview," Mol. Imag. Biol. **16**(5), 652–660 (2014).
4. C. Xu, P. D. Kumavor, U. Alqasemi, H. Li, Y. Xu, S. Zanganeh, and Q. Zhu, "Indocyanine green enhanced co-registered diffuse optical tomography and photoacoustic tomography," J. Biomed. Opt. **18**(12), 126006 (2013).
5. A. De la Zerda, C. Zavaleta, S. Keren, S. Vaithilingam, S. Bodapati, Z. Liu, J. Levi, B. R. Smith, T.-J. Ma, O. Oralkan, Z. Cheng, X. Chen, H. Dai, B. T. Khuri-Yakub, and S. S. Gambhir, "Carbon nanotubes as photoacoustic molecular imaging agents in living mice," Nat. Nanotechnol. **3**(9), 557–562 (2008).
6. X. Yang, E. W. Stein, S. Ashkenazi, and L. V. Wang, "Nanoparticles for photoacoustic imaging," Wiley Interdiscip Rev Nanomed Nanobiotechnol **1**(4), 360–368 (2009).
7. A. P. Jathoul, J. Laufer, O. Ogunlade, B. Treeby, B. Cox, E. Zhang, P. Johnson, A. R. Pizzey, B. Philip, T. Marafioti, M. F. Lythgoe, R. B. Pedley, M. a. Pule, and P. Beard, "Deep in vivo photoacoustic imaging of mammalian tissues using a tyrosinase-based genetic reporter," Nat. Photonics **9**, 239–246 (2015).
8. J. Laufer, D. Delpy, C. Elwell, and P. Beard, "Quantitative spatially resolved measurement of tissue chromophore concentrations using photoacoustic spectroscopy: application to the measurement of blood oxygenation and haemoglobin concentration," Phys. Med. Biol. **52**(1), 141–168 (2007).
9. B. Cox, J. G. Laufer, S. R. Arridge, and P. C. Beard, "Quantitative spectroscopic photoacoustic imaging: a review," J. Biomed. Opt. **17**(6), 061202 (2012).
10. J. Laufer, A. Jathoul, M. Pule, and P. Beard, "In vitro characterization of genetically expressed absorbing proteins using photoacoustic spectroscopy," Biomed. Opt. Express **4**(11), 2477–2490 (2013).
11. J. Laufer, E. Zhang, and P. Beard, "Evaluation of Absorbing Chromophores Used in Tissue Phantoms for Quantitative Photoacoustic Spectroscopy and Imaging," IEEE J. Sel. Top. Quantum Electron. **16**(3), 600–607 (2010).
12. D. Razansky, C. Vinegoni, and V. Ntziachristos, "Multispectral photoacoustic imaging of fluorochromes in small animals," Opt. Lett. **32**(19), 2891–2893 (2007).
13. C. Lutzweiler, R. Meier, E. Rummeny, V. Ntziachristos, and D. Razansky, "Real-time optoacoustic tomography of indocyanine green perfusion and oxygenation parameters in human finger vasculature," Opt. Lett. **39**(14), 4061–4064 (2014).
14. D. Razansky, M. Distel, C. Vinegoni, R. Ma, N. Perrimon, R. W. Köster, and V. Ntziachristos, "Multispectral opto-acoustic tomography of deep-seated fluorescent proteins in vivo," Nat. Photonics **3**(7), 412–417 (2009).

15. G. S. Filonov, A. Krumholz, J. Xia, J. Yao, L. V. Wang, and V. V. Verkhusha, "Deep-tissue photoacoustic tomography of a genetically encoded near-infrared fluorescent probe," Angew. Chem. Int. Ed. Engl. **51**(6), 1448–1451 (2012).
16. A. Krumholz, D. M. Shcherbakova, J. Xia, L. V. Wang, and V. V. Verkhusha, "Multicontrast photoacoustic in vivo imaging using near-infrared fluorescent proteins," Sci. Rep. **4**, 3939 (2014).
17. S. Ashkenazi, S.-W. Huang, T. Horvath, Y.-E. L. Koo, and R. Kopelman, "Photoacoustic probing of fluorophore excited state lifetime with application to oxygen sensing," J. Biomed. Opt. **13**(3), 034023 (2008).
18. E. Morgounova, Q. Shao, B. J. Hackel, D. D. Thomas, and S. Ashkenazi, "Photoacoustic lifetime contrast between methylene blue monomers and self-quenched dimers as a model for dual-labeled activatable probes," J. Biomed. Opt. **18**(5), 056004 (2013).
19. A. Penzkofer, W. Falkenstein, and W. Kaiser, "Vibronic relaxation in the S1 state of rhodamine dye solutions," Chem. Phys. Lett. **44**(1), 82–87 (1976).
20. G. Jung, J. Wiehler, and A. Zumbusch, "The photophysics of green fluorescent protein: influence of the key amino acids at positions 65, 203, and 222," Biophys. J. **88**(3), 1932–1947 (2005).
21. J. Hendrix, C. Flors, P. Dedecker, J. Hofkens, and Y. Engelborghs, "Dark states in monomeric red fluorescent proteins studied by fluorescence correlation and single molecule spectroscopy," Biophys. J. **94**(10), 4103–4113 (2008).
22. A. Penzkofer and W. Blau, "Theoretical analysis of S 1 state lifetime measurements of dyes with picosecond laser pulses," Opt. Quantum Electron. **15**, 325–347 (1983).
23. A. Danielli, C. P. Favazza, K. Maslov, and L. V. Wang, "Picosecond absorption relaxation measured with nanosecond laser photoacoustics," Appl. Phys. Lett. **97**(16), 163701 (2010).
24. R. Menzel and E. Thiel, "Intersystem crossing rate constants of rhodamine dyes: influence of the amino-group substitution," Chem. Phys. Lett. **291**(1-2), 237–243 (1998).
25. J. Märk, C. Theiss, F.-J. Schmitt, and J. Laufer, "Photoacoustic imaging of a near-infrared fluorescent marker based on dual wavelength pump-probe excitation," in Proc. of SPIE, Photons Plus Ultrasound: Imaging and Sensing, 2014, **8943**, p. 894333.
26. A. Grofcsik and W. J. Jones, "Stimulated emission cross-sections in fluorescent dye solutions: gain spectra and excited-state lifetimes of Nile blue A and oxazine 720," J. Chem. Soc., Faraday Trans. **88**(8), 1101 (1992).
27. W. Min, S. Lu, S. Chong, R. Roy, G. R. Holtom, and X. S. Xie, "Imaging chromophores with undetectable fluorescence by stimulated emission microscopy," Nature **461**(7267), 1105–1109 (2009).
28. P. Sathy, R. Philip, V. P. N. Nampoori, and C. P. G. Vallabhan, "Photoacoustic observation of excited singlet state absorption in the laser dye rhodamine 6G," J. Phys. D Appl. Phys. **27**(10), 2019–2022 (1994).
29. W. Köchner, *Solid-State Laser Engineering*, 6th ed. (Springer, 2006).
30. S. Bedö, M. Pollnau, W. Lüthy, and H. P. Weber, "Saturation of the 2.71 μm laser output in erbium-doped ZBLAN fibers," Opt. Commun. **116**(1-3), 81–86 (1995).
31. F. P. Schafer, *Principles of Dye Laser Operations in Topics in Applied Physics: Dye Laser* (Berlin: Springer, 1983).
32. E. Zhang, J. Laufer, and P. Beard, "Backward-mode multiwavelength photoacoustic scanner using a planar Fabry-Perot polymer film ultrasound sensor for high-resolution three-dimensional imaging of biological tissues," Appl. Opt. **47**(4), 561–577 (2008).
33. J. Laufer, P. Johnson, E. Zhang, B. Treeby, B. Cox, B. Pedley, and P. Beard, "In vivo preclinical photoacoustic imaging of tumor vasculature development and therapy," J. Biomed. Opt. **17**(5), 056016 (2012).
34. J. Laufer, F. Norris, J. Cleary, E. Zhang, B. Treeby, B. Cox, P. Johnson, P. Scambler, M. Lythgoe, and P. Beard, "In vivo photoacoustic imaging of mouse embryos," J. Biomed. Opt. **17**(6), 061220 (2012).
35. P. Venkateswarlu, M. C. George, Y. V. Rao, H. Jagannath, G. Chakrapani, and A. Miahnahri, "Transient excited singlet state absorption in Rhodamine 6G," Pramana **28**(1), 59–71 (1987).
36. J. P. Hermann and J. Ducuing, "Dispersion of the two-photon cross section in rhodamine dyes," Opt. Commun. **6**(2), 101–105 (1972).
37. D. Magde, R. Wong, and P. G. Seybold, "Fluorescence quantum yields and their relation to lifetimes of rhodamine 6G and fluorescein in nine solvents: improved absolute standards for quantum yields," Photochem. Photobiol. **75**(4), 327–334 (2002).
38. P. Sathy and A. Penzkofer, "Absorption and fluorescence spectroscopic analysis of rhodamine 6G and oxazine 750 in porous sol-gel glasses," J. Photochem. Photobiol. Chem. **109**(1), 53–57 (1997).
39. B. E. Treeby, E. Z. Zhang, and B. T. Cox, "Photoacoustic tomography in absorbing acoustic media using time reversal," Inverse Probl. **26**(11), 115003 (2010).
40. K. E. Sapsford, L. Berti, and I. L. Medintz, "Materials for fluorescence resonance energy transfer analysis: beyond traditional donor-acceptor combinations," Angew. Chem. Int. Ed. Engl. **45**(28), 4562–4589 (2006).
41. A. M. Brouwer, "Standards for photoluminescence quantum yield measurements in solution (IUPAC Technical Report)," Pure Appl. Chem. **83**(12), 2213–2228 (2011).

1. Introduction

Photoacoustic (PA) imaging relies on the absorption of short optical pulses by tissue chromophores to generate broadband ultrasonic waves that are detected at the tissue surface [1,2]. From the measured PA signals, images of the initial pressure distribution are then obtained using reconstruction algorithms. For excitation pulses in the visible and near-infrared wavelength region, these images typically show the vasculature since hemoglobin is the

strongest absorber. If contrast agents such as fluorophores [3,4] or absorbing compounds [5–7] are present, the image will also contain their contribution to the initial pressure distribution. Their detection and visualization typically relies on multiwavelength techniques, which involve the acquisition of images at multiple excitation wavelengths and the use of spectral unmixing methods such as model-based inversion schemes [8]. These techniques can be computationally expensive and rely on accurate *a priori* information, such as the wavelength dependence of the specific absorption coefficient, to account for the spectral and spatial distortion of the fluence [9]. In fluorophores, however, the assumption that the PA spectrum is proportional to the specific absorption spectrum is not always valid. Fluorescence emission and ground state depopulation can reduce the amount of thermalized energy, and hence PA signal amplitude, generated during the typically short (ns), high peak power excitation pulses [10,11]. Since the relative contributions of these effects are also wavelength-dependent, they can compromise the accuracy of spectral unmixing methods. Despite these limitations, multiwavelength imaging approaches have been used *in vivo* to visualize exogenous fluorescent contrast agents [12,13], and genetically expressed fluorescent proteins in small translucent organisms [14] and in subcutaneous tumor xenografts [15,16].

Only non-radiative relaxations contribute to the thermalisation of the optical energy, and hence the PA effect. While PA pump-probe excitation of methylene blue has already been used to investigate the dependence of transient absorption on oxygen concentration [17,18], the technique presented in this paper is based on modulating the excited state lifetime of fluorophores by inducing stimulated emission (SE) which, in turn, results in a nonlinear modulation of the thermalized energy, and hence the PA signal amplitude. A theoretical model of the PA signal generation in fluorophores using pump-probe excitation is presented and experimentally validated on cuvette measurements made in solutions of a fluorophore of known optical and molecular properties. The application of this technique to deep tissue tomographic PA imaging is demonstrated by determining the spatial distribution of a near-infrared fluorophore in a tissue phantom.

2. Background

2.1 PA signal generation in fluorophores

The electronic and vibrational transitions in a fluorophore during pump photon excitation are illustrated in Fig. 1(a). The absorption of a pump photon, which occurs on a timescale of fs, promotes the molecule to an excited state, S_1^*, from where it relaxes vibrationally (within ps) to the lowest level of the excited electronic state, S_1 [19]. From S_1, it then returns to the electronic ground state, S_0, either via spontaneous emission of a photon, i.e. fluorescence, or via non-radiative processes, such as vibrational decay, internal conversion, or inelastic collisions. In fluorophores, this generally occurs on much longer timescales than vibrational relaxation, ranging from hundreds of ps to several ns [20,21]. A third possible relaxation pathway from S_1 to the ground state (not shown in Fig. 1(a)) is intersystem crossing via a triplet state, which may relax via phosphorescence or non-radiative relaxation on a timescale of ms. Though formally prohibited by the laws of quantum mechanics, this transition may still be observed in large fluorescent molecules, where strong spin-orbit coupling enables such spin-flip reactions.

Only non-radiative relaxations contribute to the thermalisation of the optical energy, and hence the PA effect. Non-fluorescent tissue chromophores, such as hemoglobin, water and lipids, relax via fast non-radiative processes (within ps), i.e. the optical energy is thermalized almost completely due to vibrational dissipation. In fluorophores, by contrast, the local thermalized energy is affected by (i) fluorescence, (ii) ground state depopulation [22], and (iii) intersystem crossing, which results in time-resolved PA signals that may differ in amplitude from those generated in non-fluorescent chromophores of equal absorption coefficient. First, the emission of fluorescence reduces the local thermalized energy. Second, ground state depopulation, which is caused by long excited state lifetimes, can lead to a transient reduction in the number of molecules in the ground state during ns excitation pulses. This has been

shown to result in deviations from the linear dependence of the PA signal amplitude on absorber concentration [23], and in differences between the optical absorption and corresponding PA spectra [10]. Third, intersystem crossing may also reduce the signal amplitude since triplet state relaxation occurs on ms timescales, which does not fulfill the condition of thermal and stress confinement. However, for the fluorescent dyes used in this study, intersystem crossing is considered a weak effect [24] and is therefore neglected.

We propose to modulate the excited state lifetime of fluorescent molecules using PA pump-probe excitation, a qualitative observation of which we first reported in [25]. By selecting pump and probe wavelengths that coincide with the spectral region of maximum absorption and fluorescence emission, respectively, stimulated emission (SE) can be induced. SE accelerates the relaxation of the long-lived excited states to the ground state [26,27], which modulates the local thermal energy generated during an excitation pulse. By introducing a time delay between the pump and probe pulses, SE can be suppressed. The difference in the PA signal amplitude measured using simultaneous and time-delayed pump-probe pulses provides a contrast mechanism that is unique to fluorophores since contributions from non-fluorescent chromophores are removed.

3. Materials and methods

In section 3.1, a 1-D forward model of the PA signal generation in fluorophores using pump-probe excitation is introduced. The model predicts the PA signal amplitude as a function of input parameters such as fluorophore concentration, pump and probe fluence, fluorescence lifetime, and quantum yield. The experimental setup and the cuvette measurements are described in section 3.2 and 3.3, respectively. The setup and methods used for 3-D PA imaging of a fluorophore in a tissue phantom are presented in section 3.4.

3.1 Forward model of the PA signal generation in fluorophores using pump-probe excitation

3.1.1 Rate equations of the radiative and vibrational transitions

The electronic state of a molecule is determined by the total electron energy and the symmetry of the electron spin states. Each electronic state is subdivided into a number of vibrational and rotational energy levels associated with the motion of the atomic nuclei. A simplified schematic of the energy levels of a fluorophore is shown in Fig. 1(a). The photon absorption process is assumed to start from the ground state, S_0, a spin-paired electronic singlet state. The interaction of the fluorophore with the incident pump and probe fields are modeled assuming that significant population densities are only found in the electronic ground state, S_0, and in the first excited electronic state, S_1. The vibrationally excited energy levels of the electronic states are denoted S_0^* and S_1^*. Transitions to the triplet state as well as excited state absorption processes are not expected to play a significant role for the fluorophores used in this study and are therefore neglected [24,28]. The time dependent changes in the population densities of the energy levels can then be described by a set of rate equations [29,30].
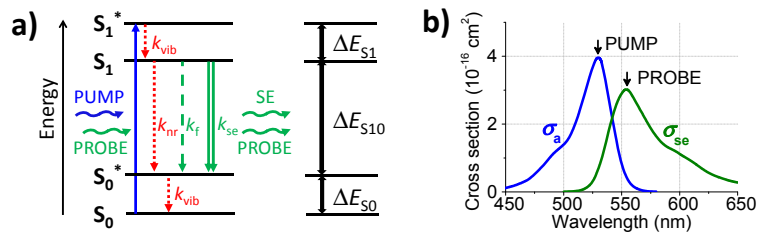

Fig. 1. (a) Schematic of the electronic and vibrational transitions in a fluorophore during pump-probe excitation (S_0 – electronic ground state, S_1 - first excited electronic state, S_0^* and S_1^* - vibrationally excited energy levels, k_{vib} - vibrational relaxation rate, k_{nr} - non-radiative relaxation rate from S_1 to S_0^*, k_f - rate of spontaneous fluorescence emission, k_{se} - rate of SE). ΔE_{S1}, ΔE_{S10}, ΔE_{S0} indicate the relative energies of the transitions. (b) Wavelength dependence of the absorption cross section, σ_a, and the SE cross section, σ_{se}, of Rhodamine 6G.

The ground state, S_0, is coupled to the vibrationally excited Franck Condon state, S_1^*, by a pump photon absorption process. The change in the respective population can be described by

$$\frac{\partial N_1^*(t)}{\partial t} = (N_0(t) - N_1^*(t))\, \sigma_a \, \Phi^R_{pump} - N_1^*(t)\, k_{vib} \qquad (1)$$

where N_1^* is the time-dependent population probability of S_1^*, N_0 is the relative population probability of S_0, σ_a is the wavelength-dependent absorption cross section in cm^2 (Fig. 1(b)), Φ^R_{pump} the pump fluence rate (in $mol\ cm^{-2}\ s^{-1}$), and k_{vib} is the vibrational relaxation rate from S_1^* to S_1. The first term describes the increase in N_1^* due to pump photon absorption, and also formally includes the possibility of SE (from S_1^* to S_0) induced by pump photons. However, this effect is unlikely to occur due to the fast vibrational relaxation from S_1^* to S_1, which is described by the second term.

The rate of transition from S_1 to S_0^* is inversely proportional to the fluorescence lifetime, τ, given by

$$\tau = \frac{1}{k_{nr} + k_f} \qquad (2)$$

where k_{nr} is the non-radiative relaxation rate, which includes vibrational transitions and collisional energy transfer, and k_f the rate of spontaneous fluorescence emission. The values of k_{nr} and k_f are of the same order of magnitude and are related through the quantum yield, η, which describes the relative probability of radiative transitions

$$\eta = k_f \tau \qquad (3)$$

The rate equation that describes the temporal change of the population at S_1 is given by

$$\frac{\partial N_1(t)}{\partial t} = N_1^*(t)\, k_{vib} - \frac{N_1(t)}{\tau} - (N_1(t) - N_0^*(t))\, \sigma_{se} \, \Phi^R_{probe} \qquad (4)$$

where N_1 is the population probability of S_1, N_0^* is the population probability at S_0^*, σ_{se} is the wavelength-dependent SE cross section in cm^2 (Fig. 1(b)), and Φ^R_{probe} is the probe fluence rate (in $mol\ cm^{-2}\ s^{-1}$). The first term describes the increase in the N_1 population due to vibrational relaxation from S_1^*, while the second term describes the reduction in N_1 due to spontaneous fluorescence emission and non-radiative relaxation processes. The third term describes the reduction in N_1 due to the stimulated emission induced by the probe pulse. As in Eq. (1), the third terms also formally includes the possibility of probe photon absorption and a transition from S_0^* to S_1, which is unlikely to occur due to fast vibrational relaxation from S_0^* to the vibrational ground state, S_0. The respective rate equations for N_0^* and N_0 are

$$\frac{\partial N_0^*(t)}{\partial t} = \frac{N_1(t)}{\tau} + (N_1(t) - N_0^*(t))\, \sigma_{se} \, \Phi^R_{probe} - N_0^*(t)\, k_{vib} \qquad (5)$$

$$\frac{\partial N_0(t)}{\partial t} = N_0^*(t)\, k_{vib} - (N_0(t) - N_1^*(t))\, \sigma_a \, \Phi^R_{pump} \qquad (6)$$

Since $k_{vib} \gg \tau^{-1}$, it is assumed that k_{vib} is the same for the vibrational transitions within the first electronically excited state and the electronic ground state. The sum of the population probabilities, $N_i(t)$, equals unity. The absolute population densities are calculated by multiplying $N_i(t)$ by the concentration of the fluorescent molecules, c (in cm^{-3}).

3.1.2 Light propagation model

The pump and probe fluence rate distributions are described as a function of depth, x, and time, t, by using the Lambert-Beer absorption law for an optically homogeneous, non-scattering medium. The pump fluence rate distribution is given by

$$\Phi^R_{\text{pump}}(x,t) = \Phi^R_{0\text{pump}} \, G(t) \, e^{-\mu_a(x,t)\,x} \tag{7}$$

Similarly, the probe fluence rate distribution can be expressed as

$$\Phi^R_{\text{probe}}(x,t) = \Phi^R_{0\text{probe}} \, G(t) \, e^{-\mu_{se}(x,t)\,x} \tag{8}$$

where $G(t)$ is a Gaussian function that describes the time course of the excitation pulses. Its full-width-half-maximum corresponds to the pulse duration. $\Phi^R_{0\,\text{pump}}$ and $\Phi^R_{0\,\text{probe}}$ are the fluence rate values at the surface of the sample. $\mu_a(x,t)$ and $\mu_{se}(x,t)$ are the depth- and time-dependent absorption and SE coefficients, respectively, and are given by

$$\mu_a(x,t) = (N_0(x,t) - N_1^*(x,t))\,c\,\sigma_a, \tag{9}$$

$$\mu_{se}(x,t) = (N_0^*(x,t) - N_1(x,t))\,c\,\sigma_{se} \tag{10}$$

To describe the light propagation, the depth dependence of the populations, i.e. $N_i(x,t)$, is introduced. In order to calculate $\mu_a(x, t)$ and $\mu_{se}(x, t)$, Eqs. (9) and (10) are inserted in Eqs. (7) and (8), and the expressions for the pump and probe fluence rates are inserted into the coupled differential population rate Eqs. (1), (4), (5) and (6).

3.1.3 Calculation of the PA signal

In non-fluorescent chromophores, which typically exhibit rapid, non-radiative relaxation, the ground state can be considered fully populated during the excitation pulse, i.e. $N_0(x, t) = 1$. In this case, $\mu_a(x, t)$ is constant. For the case of negligible absorption at the probe wavelength, the initial pressure p_0 is then given by

$$p_0(x) = \Gamma \int_{pulse} \mu_a \, \Phi_{\text{pump}}(x,t) \, dt \tag{11}$$

where Γ is the Grüneisen coefficient, which is a measure of the conversion efficiency of absorbed energy to pressure and Φ_{pump} the pump fluence (in photons cm^{-2}). The excitation pulse is assumed to correspond to a temporal delta function.

In fluorescent molecules, the thermalized energy is affected by i) fluorescence emission, and ii) the space- and time-dependent population densities $N_i(x, t)$, which in turn determine $\mu_a(x, t)$ and $\mu_{se}(x, t)$. The initial pressure is therefore proportional to the number of vibrational and non-radiative transitions weighted by their relative energy level difference (as illustrated in Fig. 1(a)) integrated over the duration of the excitation pulses. The following expression then describes the initial pressure p_0 as a function of penetration depth

$$p_0(x) = \Gamma c \int_{pulses} \left(\left(\frac{\Delta E_{S1}}{E} \right) N_1^*(x,t)\, k_{vib} + \left(\frac{\Delta E_{S10}}{E} \right) \left(\frac{N_1(x,t)}{\tau} \right)(1-\eta) + \left(\frac{\Delta E_{S0}}{E} \right) N_0^*(x,t)\, k_{vib} \right) dt \tag{12}$$

where ΔE_{S1} and ΔE_{S0} is the amount of energy that is thermalized due to the vibrational transitions from S_1^* to S_1 and S_0^* to S_0, respectively. ΔE_{S10} is the energy of the transition from S_1 to S_0^*, and E is the energy of the transition S_0 to S_1^*, i.e. the energy of the absorbed pump photon. The energy level of S_1 can be estimated from the wavelength at which the absorption and fluorescence spectra intersect [31].

By solving the system of coupled rate equations, the initial pressure can be calculated using Eq. (12). The output of the forward model is the time-resolved PA signal amplitude,

$S(t)$, which is a function of fluorophore concentration, pump and probe fluence, pump-probe pulse time delay, Δt, and speed of sound, c_s, in the sample:

$$S(t) = K \, f(c, \Phi_{pump}(\lambda), \Phi_{probe}(\lambda), \Delta t, c_s, t - t_0) \qquad (13)$$

where Φ_{probe} is the probe fluence (in photons cm^{-2}), t_0 is the acoustic transit time between the illuminated surface of the sample and the acoustic detector. K is a scaling factor, which includes factors such as acoustic attenuation, the sensitivity of the transducer, and signal amplification. Fixed model input parameters are $\sigma_a(\lambda)$, $\sigma_{se}(\lambda)$, k_{vib}, k_f, k_{nr}, ΔE_{S1}, ΔE_{S0}, and ΔE_{S10}.
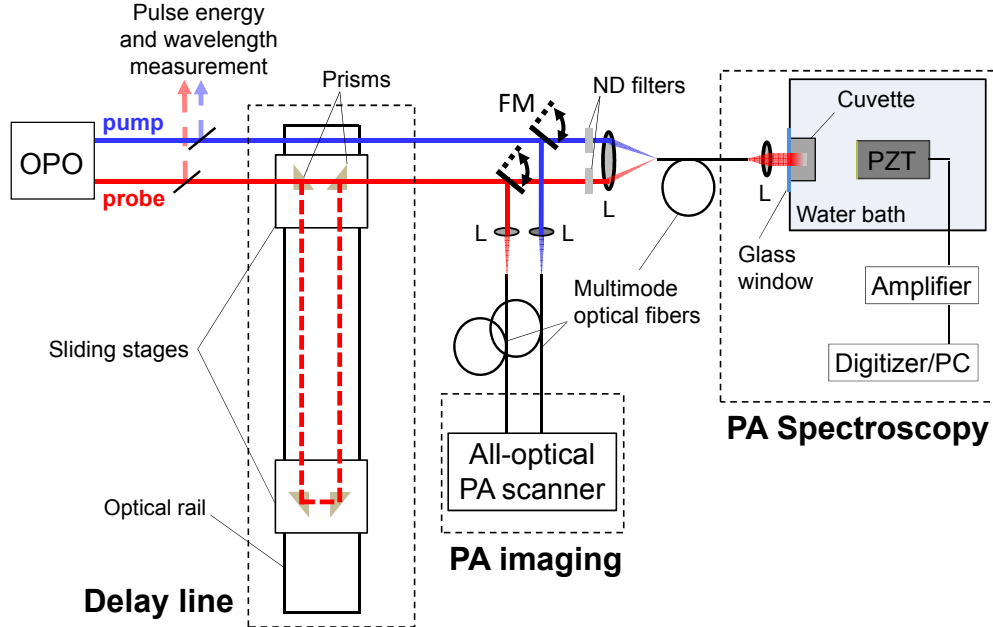
3.2 Experimental setup

Fig. 2. Experimental setup for (i) measuring PA signals in a cuvette and (ii) acquiring tomographic PA images using time delayed pump and probe excitation pulses (PZT - piezoelectric ultrasound transducer, FM - flipper mirror, L - lenses).

The generation of PA signals in fluorophore solutions using pump-probe excitation was investigated (i) by making measurements in cuvettes using PA spectroscopy and (ii) by acquiring 3-D tomographic images in a tissue phantom using an all-optical PA imaging system. A schematic of the experimental setup is shown in Fig. 2. A wavelength tunable OPO laser system (Newport Spectra Physics, USA) provided pump and probe excitation pulses of 7 ns duration at a repetition frequency of 50 Hz. Small portions of the excitation pulses were directed to an integrating sphere to measure the pulse energy with a wavelength-calibrated photodiode/integrator system and the wavelength with an USB spectrometer (Ocean Optics, USA). Prism reflectors mounted on an optical rail were used to control the time delay between the pump and probe pulses ($\Delta t = 0.0 - 7.7$ ns).

For the cuvette measurements, the signal and idler outputs of the OPO were coupled into a single fiber (1.5 mm core dia.) to homogenize and co-align the pump and probe beams. The output of the fiber was collimated and directed onto a custom made cuvette (5 mm path length) placed in a water bath. The beam diameter was approximately 4.5 mm. Neutral density (ND) filters were used to control the fluence. PA signals were detected using a planar piezoelectric transducer with a 10 MHz center frequency (Precision Acoustics, UK),

amplified with a 40 dB voltage preamplifier (Femto, Germany), and recorded using a digitizer card (National Instruments, USA). For the PA imaging experiments in tissue phantoms, the output of the OPO was coupled into two separate fibers (1.5 mm core dia.) to direct the pump and probe pulses to an all-optical PA scanner based on a Fabry-Pérot etalon ultrasound sensor, which is described in detail elsewhere [32–34]. The PA imaging experiments are described in section 3.4.

3.3 Cuvette measurements

PA signals were measured using (a) pump pulse excitation, (b) probe pulse excitation, and (c) simultaneous pump and probe pulse excitation. The signals obtained in (a) and (b) were added and are subsequently referred to as 'signal without SE' while the signal obtained using simultaneous pump and probe pulses is referred to as 'signal with SE'. Figure 3 illustrates the initial compressive part (corresponding to the positive pressure generated in the absorbing sample in the cuvette) of a set of typical time-resolved PA signals. The signals were calculated using the forward model (Eq. (13)). The peak amplitude of a signal generated without SE is reduced compared to that generated in a non-fluorescent absorber of the same μ_a due to the effects of fluorescence emission and ground state depopulation [22,23]. By contrast, a signal generated with SE can exhibit an increase in the peak signal amplitude. By subtracting the signals with and without SE, a difference signal is obtained. Its amplitude provides a measure of the change in the local thermalized energy due to SE and its effect on the excited state lifetime.
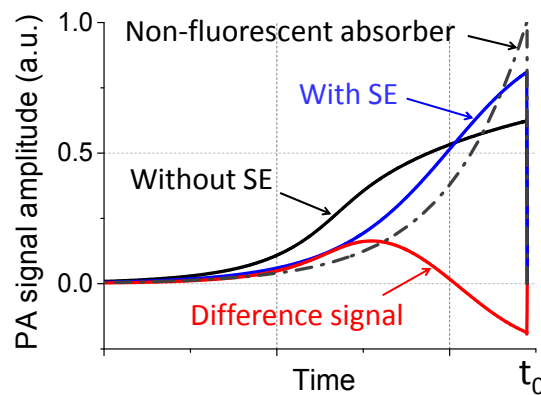

Fig. 3. Illustration of the initial compressive part of time-resolved PA signals generated in (i) a non-fluorescent absorber (grey dashed line), (ii) a fluorophore with SE (blue line), i.e. simultaneous pump and probe pulses, and (iii) a fluorophore without SE (black solid line), i.e. separate pump and probe pulses. A difference signal (red line), which provides a measure of the change in the local thermalized energy, is obtained by subtracting (ii) and (iii). The signals were predicted using the forward model (Eq. (13)).

PA signals were measured in solutions of rhodamine 6G (Santa Cruz Biotechnology, USA) in methanol in a cuvette. Rhodamine 6G (R6G) is a fluorophore with well-known optical properties, such as radiative and non-radiative decay rates, and absorption and SE cross sections (Fig. 1(b)) [35–38]. Its quantum yield is 0.9 and the fluorescence lifetime is 3.9 ns. For the measurements on R6G solutions, the pump and probe wavelengths were 532 nm and 560 nm, respectively. The R6G concentrations ranged from 42.5 to 170 µM (μ_a = 1.2 - 4.6 mm^{-1} at 532 nm). No evidence of photobleaching was found during the experiments. PA signals were measured in R6G solutions as a function of i) pump and probe fluence, ii) R6G concentration, iii) probe wavelength, and iv) time delay between the pump and probe pulse.

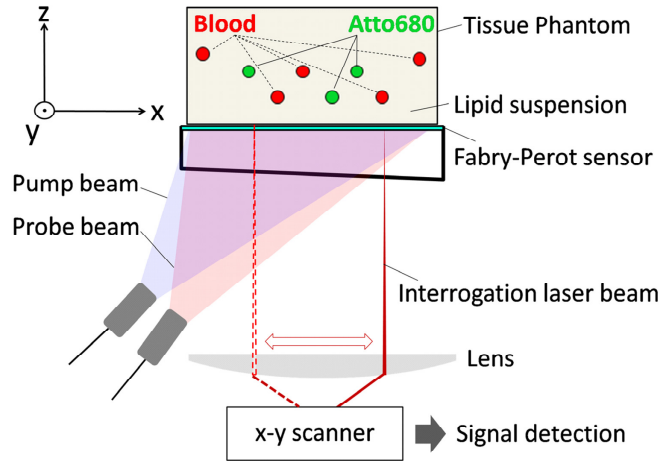*3.4 PA difference imaging of a tissue phantom*

Fig. 4. Experimental setup for tomographic PA imaging of a tissue phantom, which consisted of capillary tubes filled with an aqueous solution of Atto680 (c = 160 µM) or blood immersed in a scattering lipid suspension. Image data sets were acquired in backward mode using a Fabry-Pérot based PA scanner using simultaneous and time delayed (Δt = 7.7 ns) pump-probe pulses.

The PA imaging setup is shown in Fig. 4. The tissue phantom was illuminated through the transparent Fabry-Pérot ultrasound sensor by the divergent output of the optical fibers, which produced a beam diameter of approximately 2 cm at the phantom surface. It consisted of a scattering lipid suspension (μ_s' ~1.5 mm^{-1}) in which polymer capillary tubes (i.d. 600 µm, Paradigm Optics Inc., USA) were immersed. The tubes were filled with a fluorescent dye, Atto680 (Atto-tec GmbH, Germany) in aqueous solution (c = 160 µM, μ_a = 4.6 mm^{-1} at 680 nm), or whole murine blood. Atto680 in water has a fluorescence lifetime of 1.7 ns and a quantum yield of 0.3. 3-D tomographic image data sets were acquired in backward mode using a pump fluence of 6 mJ/cm^2 at a wavelength of 680 nm and a probe fluence of 7 mJ/cm^2 at 742 nm. The *x-y* scan area was 22 mm by 4 mm. Two image data sets were acquired using (i) simultaneous pump-probe pulses and (ii) time delayed pump and probe pulses (Δt = 7.7 ns). Images of the initial pressure distribution were reconstructed using a time reversal image reconstruction algorithm [39]. A difference image was obtained by subtracting the images acquired using simultaneous and time delayed pulses.

4. Results

4.1 Cuvette measurements in R6G solutions

4.1.1 Effect of pump and probe fluence

Figure 5 shows the initial compressive part of PA signals measured in an 85 µM R6G solution using different pump and probe pulse fluences together with signals calculated using the forward model. The model input parameters were the known concentration, the measured pump and probe fluences, and the optical properties of R6G, such as $\sigma_a(\lambda)$, $\sigma_{se}(\lambda)$, k_{vib}, and k_f [35–38]. Figure 5(a) shows the PA signals for Φ_{pump} = 10 mJ/cm^2 and Φ_{probe} = 28 mJ/cm^2. Figure 5(b)-5(d) (left column) show the PA signals for decreasing Φ_{pump} at constant Φ_{probe}, while Fig. 5(e)-5(g) (right column) show the PA signals for decreasing Φ_{probe} at constant Φ_{pump}. In Fig. 5(a), the PA signal without SE does not show the typical exponential shape observed in non-fluorescent absorbers. The PA signal amplitude at t_0 = 4.45 µs, which corresponds to the region adjacent to the cuvette window, is lower than that at earlier times points around 4.2 µs, i.e. corresponding to deeper regions. This suggests that ground state

depopulation is strong for high pump fluences. Under such conditions, a significant portion of the pump photons encounter molecules in an excited state and are therefore not absorbed.
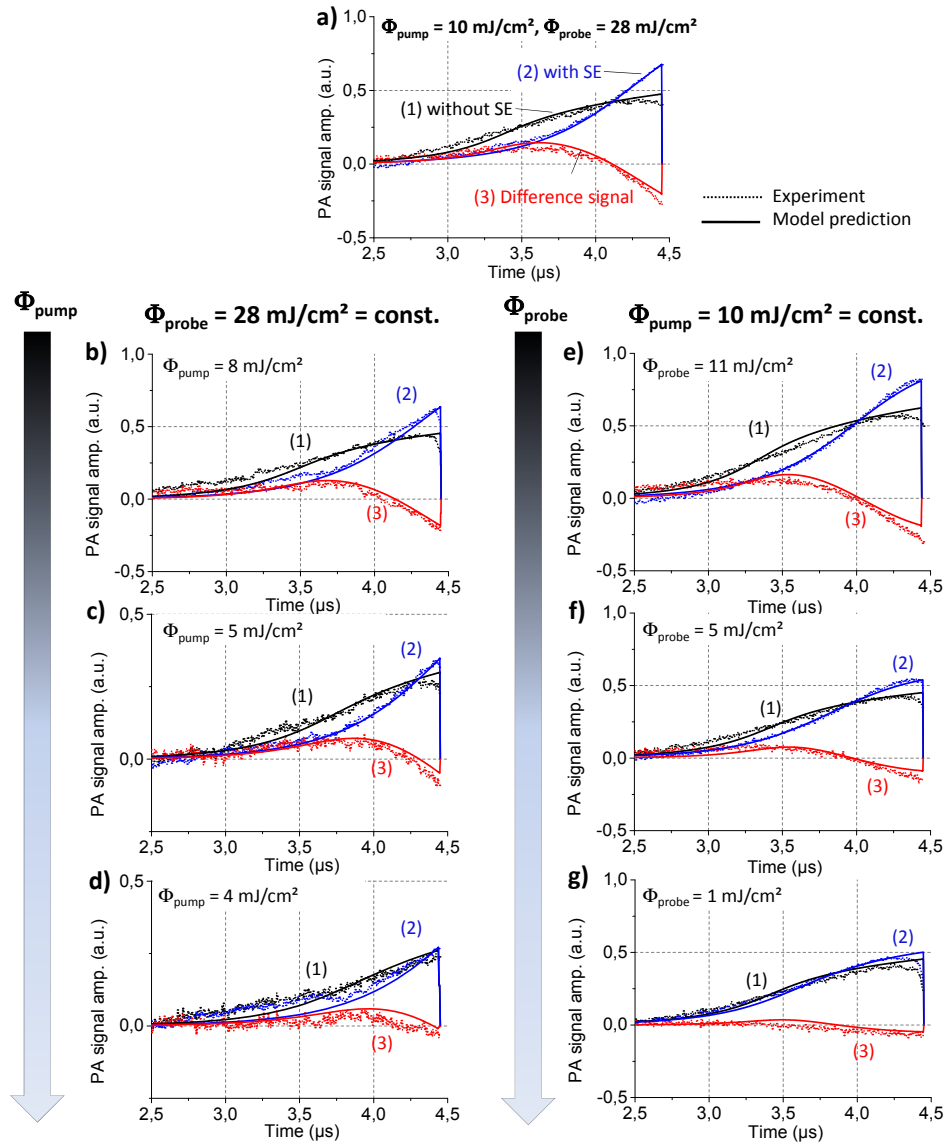

Fig. 5. PA signals measured in R6G solutions ($c = 85$ μM) in a cuvette (dotted lines) and those predicted by the forward model (solid lines) for different pump-probe fluences ($t_0 = 4.45$ μs). The black lines correspond to the signal without SE (1), the blue lines correspond to the signal with SE (2) and red line represents the calculated difference signal (3).

These photons will propagate further into the sample, resulting in increased PA amplitude at greater depths. By contrast, the signal with SE has higher peak amplitude and is almost exponential in shape. This is because SE causes rapid relaxation to the ground state, which allows the repeated absorption and thermalisation of additional pump photons. The changes to the local thermalized energy are also evident from the difference signal, which shows negative amplitude close to the cuvette surface, i.e. an increase in thermalized energy, and positive amplitude at larger penetration depths, i.e. a reduction in thermalized energy. Figure

5(b)-5(d) show the effect of decreasing Φ_{pump}, which decreases the difference signal amplitude. In addition, the shape of the PA signal without SE gradually approaches that of an exponential function. This suggests that ground state depopulation is less significant at low pump fluences. In this situation, the density of pump photons is sufficiently low to result predominately in ground state absorption. Figure 5(e)-5(g) show that by reducing Φ_{probe} while keeping Φ_{pump} constant the PA difference signal amplitude, and hence the effect of SE, is reduced. The experimental and the modeled data are in good agreement.

4.1.2 Effect of concentration

Figure 6 shows PA signals measured in R6G solutions with concentrations of 42.5 µM, 85 µM, and 170 µM. At 170 µM (Fig. 6(a)), the pump pulse (Φ_{pump} = 6 mJ/cm^2) is strongly absorbed as evidenced by the fast exponential increase in the PA signal amplitude. In addition, the difference between the signals acquired with and without SE (for Φ_{probe} = 24 mJ/cm^2) is small compared to those at lower concentrations. At high concentrations, the pump photon density per fluorescent molecule is sufficiently low to prevent ground state depopulation, i.e. most pump photons encounter molecules in the ground state. The fluence distribution is therefore similar to that predicted by the Beer-Lambert law. In addition, the effects of SE are minimal since repeated absorption-relaxation cycles are unlikely. With decreasing concentration, the relative amplitude of the difference signal compared to the signal without SE increases from 15% at 170 µM (Fig. 6(a)), to 40% at 85 µM (Fig. 6(b)), and to almost 90% at 42.5 µM (Fig. 6(c)). At low concentrations, the pump photon density per fluorescent molecule is sufficiently large for ground state depopulation to occur, which in turn allows SE, and its effect on the thermalized energy, to become more evident. The measured signals and those predicted by the model are in good qualitative agreement in terms of the relative signal amplitudes with only minor differences observed in the signal shape.
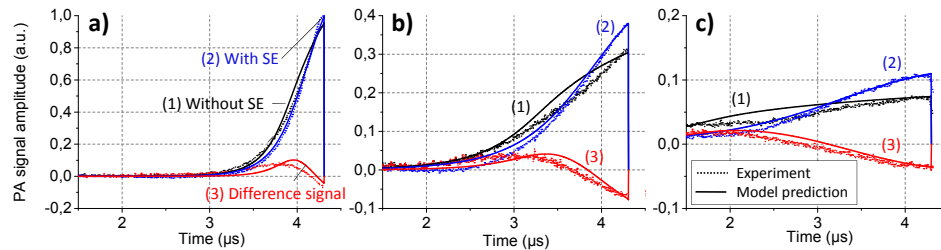

Fig. 6. PA signals measured in R6G solutions of different concentration (dotted lines) and those predicted by the forward model (solid lines): (a) 170 µM, (b) 85 µM, and (c) 42.5 µM. The pump fluence was 6 mJ/cm^2, the probe fluence was 24 mJ/cm^2, and t_0 was 4.3 µs.

4.1.3 Effect of probe wavelength

Figure 7(a) shows the difference signal amplitude (peak-to-peak) measured in R6G solution as a function of probe beam wavelength for constant pump-probe fluences together with that predicted by the forward model. The maximum difference signal was measured at a probe wavelength of 560 nm, which is close to the wavelength of maximum fluorescence emission. The difference signal decreases with increasing wavelength according to $\sigma_{se}(\lambda)$ of R6G, with experimental and modeled data showing good agreement. It was found that the agreement between model and data was improved further by selecting a quantum yield of 0.93, comparable to the value measured in ethanol solutions of R6G [37].

4.2 Effect of pump-probe time delay

Figure 7(b) shows the difference signal amplitude (peak-to-peak) measured in an R6G solution as a function of time delay together with the model prediction (c = 170 µM, Φ_{pump} = 4 mJ/cm^2, and Φ_{probe} = 10 mJ/cm^2). The difference signal decreases with increasing time delay,

which is explained by the gradual suppression of SE. The measured and modeled data were found to be in good agreement.
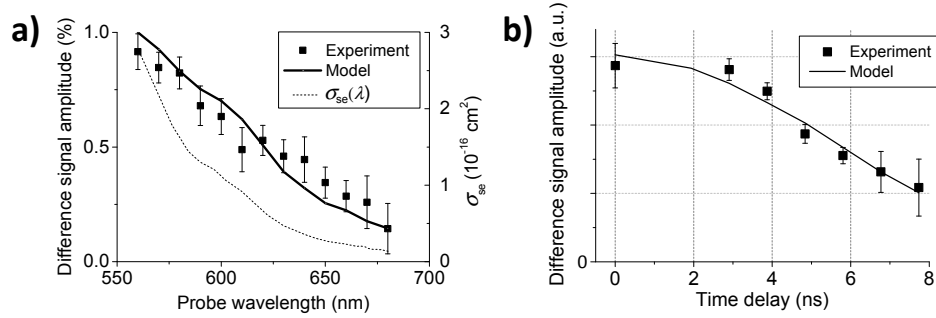

Fig. 7. (a) Difference signal amplitude (peak-to-peak) measured in R6G as a function of probe pulse wavelength together with the model prediction (c = 85 µM, Φ_{pump} = 9 mJ/cm^2, Φ_{probe} = 16 mJ/cm^2). $\sigma_{se}(\lambda)$ is shown for comparison. (b) Difference signal amplitude (peak-to-peak) measured in an R6G solution as a function of time delay together with the model prediction (c = 170 µM, Φ_{pump} = 4 mJ/cm^2, Φ_{probe} = 10 mJ/cm^2). The error bars in (a) and (b) correspond to the standard deviation of three measurements.

4.3 PA difference imaging of fluorophores in a tissue phantom

Figure 8 shows the results of the tissue phantom imaging experiments. Figure 8(a)-8(c) show 2-D *x-z* cross sectional images of 3-D image data sets acquired using simultaneous pump-probe pulses (Fig. 8(a)), time delayed pump-probe pulses (Fig. 8(b)), from which a difference image was calculated (Fig. 8(c)). While Fig. 8(a) and 8(b) show the locations of all tubes, the difference image clearly shows the location the fluorescent dye. Importantly, the background signal originating from non-fluorescent absorbers, such as blood, is removed. From the 3-D image data sets corresponding to Fig. 8(b) and 8(c), a fused volume rendered 3-D image was created using ZIBAmira (Zuse Institut Berlin, Germany) to visualize the spatial distribution of the fluorophore and that of blood (Fig. 8(d)).

5. Discussion

This study demonstrated that pump-probe excitation can be used to modulate the PA signal amplitude in fluorophores. The relative amplitude of the difference signal provided a measure of the modulation of the thermalized energy as a result of SE and was shown to depend strongly upon the ratio of fluorophore concentration and the local pump and probe fluences. In addition, the amplitude of the difference signal has been shown to depend on the cross section of SE and the pump-probe time delay.

The physical mechanism underlying the modulation of the PA signal amplitude using pump-probe excitation is the induction of SE, which strongly reduces the typically long excited state lifetime of fluorophores, accelerates the return of the molecules to the ground state, and therefore facilitates the absorption of additional pump photons during an excitation pulse. Under conditions of high probe fluence, i.e. efficient generation of SE, the number of absorption-relaxation cycles within the duration of an excitation pulse is primarily dependent upon the ratio of fluorophore concentration, c, and pump fluence, Φ_{pump}. For low c/Φ_{pump}, strong ground state depopulation and SE can result in multiple excitation-relaxation cycles during a ns excitation pulse. This accumulatively increases the amount of the local thermalized energy originating from the vibrational relaxations within the S_1 and S_0 states (Fig. 1(a)).
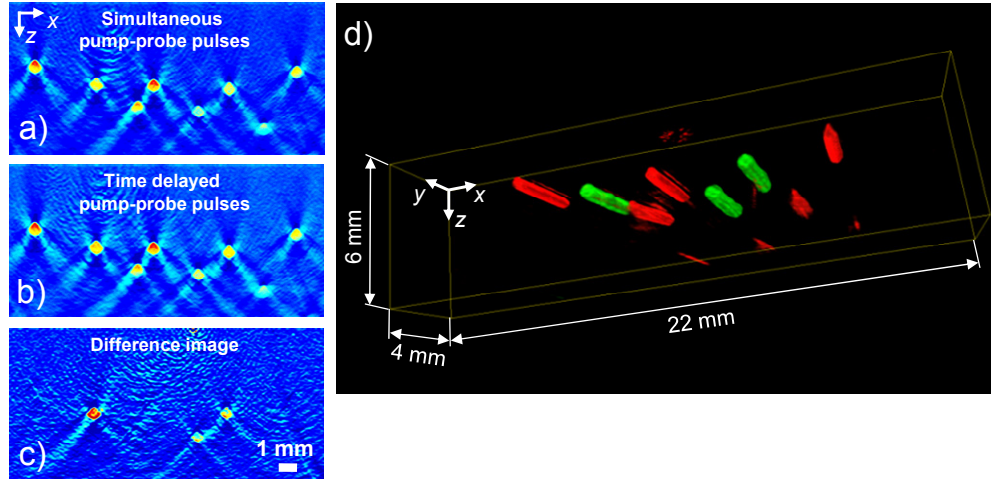
Fig. 8. Difference imaging of a tissue phantom consisting of polymer capillaries filled with Atto680 ($c = 160$ μM) and whole murine blood immersed in a scattering medium. 2-D x-z cross sectional images of 3-D PA image data sets acquired using (a) simultaneous pump-probe pulses, (b) time delayed pump-probe pulses, and (c) the difference image obtained by subtracting (b) and (c). (d) Fused volume-rendered 3-D image of (b) and (c).

This is observed as increase in the PA signal amplitude near the source where multiple absorption-relaxation cycles are supported by a high Φ_{pump}, while the attendant increase in pump photon absorption and reduction in absorption-relaxation cycles lead to a decrease in signal amplitude at greater depths (Fig. 5(a)). For large c/Φ_{pump}, by contrast, ground state depopulation is comparatively weak since most pump photons will encounter molecules in the ground state while SE reduces the number of excited molecules that may otherwise have undergone non-radiative relaxation. Since multiple excitation-relaxation cycles are unlikely to occur under these conditions, SE results in a reduction in the amount of thermalized energy, and hence the PA signal amplitude. While a difference signal can be detected in both cases, *in vivo* PA imaging applications typically result in a combination of low fluorophore concentrations and high fluence, i.e. simultaneous pump-probe pulses would produce an increase in the PA signal amplitude compared to that generated using time-delayed pulses.

The output of a forward model of the PA signal generation in R6G solutions was found to be in good agreement with the measured data, thus experimentally validating the model. It should be noted that the fitting of model input parameters, apart from the normalization of the model predictions to the measured data, was not required to achieve good agreement, i.e. the relative PA signal amplitudes were accurately predicted by the model. This suggests that a rate equation model of the temporal changes in the population density of four energy states can be used to describe the PA signal generation in fluorophores. Small discrepancies between the measured and predicted PA signals were nevertheless observed. These can be attributed to uncertainties in the measurement of experimental parameters, such as the pulse energies, and differences between the fixed model input parameters and their true values, such as the beam profile and beam divergence. A minor adjustment of the quantum yield of R6G was found to improve the agreement between model and data, which is reasonable since the optical properties, such as the quantum yield, of most fluorophores are sensitive to environmental parameters, e.g. concentration, pH, oxygen saturation [40], and deviations from literature values on the order of a few percent are not uncommon [41].

Tomographic PA imaging of a near-infrared fluorophore using pump-probe excitation in tissue phantoms was demonstrated using fluences below the ANSI safety limit of maximum permissible exposure (MPE) of skin. This method provides a PA contrast mechanism that is unique to fluorophores and can therefore be exploited for their detection. For example, multiplexed imaging of fluorophores could be achieved using a combination of wavelength

selective and pump-probe PA excitation. By calculating difference images, the PA contrast originating from non-fluorescent, endogenous absorbers is completely removed. This provides a detection method that is, in principle, limited by the noise floor of the PA image acquisition system. By contrast, the accuracy of fluorophore distributions recovered from multiwavelength images using spectral unmixing methods can also be adversely affected by uncertainties in the *a priori* information, such as the specific absorption spectra of fluorophores [10]. A further major advantage of this method lies in its simple experimental implementation, which requires the acquisition of two images with and without time delay between the pump and probe pulses, and the calculation of a difference image. In addition, the absorption and SE (or fluorescence) spectra of the near-infrared fluorophore coincide with the wavelength region where the optical penetration depth of biological tissue is at a maximum. Lastly, by detecting the spatial distribution of a fluorophore, this method may provide prior information for model-based inversion schemes for quantitative PA imaging with which the scale of the inverse problem could be reduced.

6. Conclusions

This study has demonstrated that dual wavelength pump-probe excitation can be used to induce SE in fluorescent molecules, which modulates the amount of thermalized energy, and thus the PA signal amplitude. A forward model of the PA signal generation in fluorophores based on rate equations was used to predict time-resolved signals generated in a cuvette which were found to be in good agreement with measured data. By acquiring tomographic PA difference images of a tissue phantom using pump-probe excitation, it was demonstrated that this contrast mechanism can be used to detect the location of fluorophores. This method may be suitable for *in vivo* PA imaging applications, such as preclinical imaging of exogenous or genetically expressed fluorescent labels in small animals.

Acknowledgments